

Progenitor Type Identification for Supernova Remnant N103B in the Large Magellanic Cloud by Suzaku and Chandra Observations

Kentaro SOMEYA^{1,2}, Aya BAMBA³, and Manabu ISHIDA²

¹*SoftBank Telecom Corp., 1-9-1 Higashi-shimbashi, Minato-ku, Tokyo 105-7316, Japan*

²*Institute of Space and Astronautical Science, Japan Aerospace Exploration Agency, 3-1-1 Yoshinodai, Chuo, Sagami-hara, Kanagawa 252-5210, Japan*

³*Department of Physics and Mathematics, Aoyama Gakuin University, 5-10-1 Fuchinobe, Chuo, Sagami-hara, Kanagawa 252-5258, Japan*
bamba@phys.aoyama.ac.jp

(Received 2000 December 31; accepted 2001 January 1)

Abstract

This paper presents a detailed analysis of supernova remnant (SNR) N103B located in the Large Magellanic Cloud (LMC), based on Suzaku and Chandra observations. The spectrum of the entire remnant was closely reproduced using three interstellar medium (ISM) components with temperatures of ~ 0.32 , ~ 0.56 , and ~ 0.92 keV and one ejecta component with a temperature of ~ 3.96 keV, based on spectral analysis of the Suzaku/X-ray Imaging Spectrometer (XIS) data. The ejecta was overabundant in heavy elements, such as Mg, Si, S, Ca, Fe, and Ni. The unprecedentedly high quality of data obtained by Suzaku/XIS, allowed us to correctly distinguish between the emissions from the ISM and the ejecta for the first time in a spectral analysis. Combining spectral analysis based on Suzaku/XIS data with image analysis based on Chandra/Advanced CCD Imaging Spectrometer (ACIS) data, we verified that the ejecta distributions for elements from Si to Fe-K were similar to one another, although Fe-K emission was located slightly inward compared with that of lighter elements such as Si, S, Ar, and Ca. The onion-like structure of the ejecta was maintained after the supernova explosion. In addition, the ISM emission represented by O and Fe-L was located inside the ejecta emission. We compared hydrogen-rich ejecta plasma (called “H-dominated plasma”), which is indicative of Type II SNRs, with plasma rich in heavy elements and poor in hydrogen (called “pure metal plasma”), which is mainly observed in Type Ia SNRs. In the case of N103B, we could not determine whether the origin of the continuum emission in the 4.0–6.0 keV band was from ejecta (H-dominated plasma) or high-temperature ISM (pure metal plasma) only based on the spectral modeling of Suzaku/XIS data. High-energy continuum images in the 5.2–6.0 keV band obtained by Chandra/ACIS were extremely similar to those of ejecta, implying that the origin of the high-energy continuum might indeed be the ejecta. By combining spectral analysis with high-energy continuum images, we found some indications for H-dominated plasma, and as a result, that the progenitor of N103B might have been a Type II supernova. The progenitor mass was estimated to be $13 M_{\odot}$ based on the abundance patterns of Mg, Fe, and Ni relative to Si.

Key words: ISM: individual (N103B) — shock waves — supernova remnants — X-ray: ISM

1. Introduction

A major challenge in modern astronomy is to elucidate the chemical evolution in the universe. Heavy elements are distributed throughout the universe mainly by supernova explosions, which are classified into two basic types: core collapse (CC) of massive stars (Type Ib, Ic, and II) and thermonuclear runaway of white dwarfs (Type Ia). Supernova explosions play an important role in chemical evolution being responsible for the distribution of heavy elements inside a galaxy, yielding the O group in the case of CC and the Fe group in the case of Type Ia. Accordingly, studying supernova remnants (SNRs) is essential. Typical SNRs are bright sources in the X-ray band due to the presence of high-temperature plasma ($\sim 10^7$ K) heated by the blast wave. Through X-ray observations, we can gather information about the

progenitor from the ejecta heated by the reverse shock as well as information about the surrounding environment from ISM heated by the forward shock. Such information is expected to provide insights into galactic chemical evolution and star formation history.

During SNR evolution, the X-ray emission from a young SNR at the start of the Sedov phase is complex since it is composed of emission from both ISM and ejecta. To estimate physical parameters such as plasma ionization age, number density, and plasma abundance, we need to distinguish between emissions from ISM and ejecta through image and/or spectral analysis. However, the number of young SNRs for which we can separate these components is limited. Currently, several in-orbit X-ray satellites possess high-quality spectroscopic capabilities and large effective area, (such as Suzaku and XMM-Newton) or superior imaging capabilities (such as Chandra). These satellites

allow us to study complex emissions from young SNRs.

The distance to the Large Magellanic Cloud (LMC) is 48 kpc (Macri et al. 2006), and interstellar absorption for SNRs in the LMC has a relatively small column density ($\sim 10^{21}$ Hcm²) compared with most Galactic SNRs. These properties are advantageous for estimating the physical parameters of the plasma and determining the progenitor type. The growing abundance of high-quality observation data provided by Suzaku, XMM-Newton, and Chandra warrants a re-examination of research on SNRs in the LMC. In this paper, we present the results of a study of the bright young SNR N103B in the LMC. N103B is one of the bright radio and X-ray SNRs in the LMC, and it was identified as an SNR based on its non-thermal spectrum in radio observations (Mathewson et al. 1983). Rest et al. (2005) estimated the age of N103B to be 860 yr based on the light echo, making this remnant one of the younger SNRs in the LMC. Despite being the subject of many X-ray observations (e.g., ASCA (Hughes et al. 1995), XMM-Newton (van der Heyden et al. 2002), and Chandra (Lewis et al. 2003)), the progenitor type and emission origin for this remnant are not well understood. Chu & Kennicutt (1988) reported that there is the HII region DEM L84 and the young rich cluster NGC1850 close to N103B, which suggest a CC origin. Observations with the Reflection Grating Spectrometer (RGS) onboard XMM-Newton by van der Heyden et al. (2002) also indicated that the origin might be CC, based on the O, Ne, and Mg emissions. Nevertheless, Badenes et al. (2009) suggested that N103B might have had a relatively younger and more massive Type Ia progenitor that underwent substantial mass loss before the explosion. Lewis et al. (2003) also suggested a Type Ia progenitor based on the large mass corresponding to Fe. In a recent observation, Lopez et al. (2011) conducted a statistical image analysis and reported that the progenitor was Type Ia based on the morphologies of Si XIII and 0.5–2.1 keV band emissions. Yang et al. (2013) also suggested a Type Ia progenitor based on the Cr/Mn ratio. The origin of the emission is also unclear. For instance, the O emission has been attributed to ambient material (Lewis et al. 2003) and ejecta (van der Heyden et al. 2002).

In this paper, we present the X-ray spectrum and images of N103B obtained with Suzaku and Chandra, respectively. Detailed observations and data reduction are described in § 2. Spectral analysis results are summarized in § 3. Owing to the high-quality spectra acquired by Suzaku, we were able to distinguish between emissions from ISM and ejecta, and successfully determined the abundances for the first time in a spectral analysis. In §4, we present image analysis performed using data from Chandra. On the basis of these results, we discuss the plasma parameter and the progenitor type in §5. A summary is given in §6.

2. Observation & Data Reduction

2.1. Suzaku

N103B was observed by Suzaku (Mitsuda et al. 2007) on August 30–31, 2005, as one of the Science Working Group targets. The observation log is summarized in Table 1. Suzaku is equipped with four X-ray CCD cameras (X-ray Imaging Spectrometer (XIS) 0, 1, 2, and 3: Koyama et al. (2007)) in the focal planes of the four X-ray telescopes (XRTs: Serlemitsos et al. (2007)), whose half-power diameters are $\sim 1.8'$ – $2.3'$. XIS 0, 2, and 3 are equipped with front-illuminated (FI) CCDs with high sensitivity in the high energy band, whereas XIS 1 is a back-illuminated (BI) CCD with superior sensitivity and spectral resolution at low energies (below ~ 1 keV). XIS instruments were operated in normal full-frame clocking mode without spaced-row charge injection (Nakajima et al. 2008; Uchiyama et al. 2009).

We analyzed the data taken in the 5×5 and 3×3 editing mode with revision 2.0 of the HEADAS 6.5.1 software package. In screening the data, we removed the time intervals corresponding to the South Atlantic Anomaly and night-earth and day-earth elevation angles less than 5° and 20° , respectively. We utilized only events with a grade of 0, 2, 3, 4, and 6 in the following spectral analysis. The total exposure was ~ 33 ks.

2.2. Chandra

The spatial structure of this remnant cannot be examined reliably with the image performance of Suzaku/XRT, whose half-power diameter is $\sim 2'$, since N103B has a small radius of $\sim 15''$. We therefore performed image analysis using Chandra data to facilitate the spectral analysis of the Suzaku/XIS data for the entire remnant. N103B (ObsID 1045) was observed with the Advanced CCD Imaging Spectrometer (ACIS) onboard Chandra on December 4, 1999 (see also Lewis et al. (2003)). The observation was conducted in FAINT mode. We began our analysis from Level 2 event files processed with calibration data in CALDB version 3.4.1. The observation data were not contaminated by background flares, and therefore we used the full exposure of ~ 41 ks. In the following image analysis, narrow-band images were extracted using the DMCOPY command in the Chandra Interactive Analysis of Observations (CIAO) software package version 4.1.2, and we verified the nominal energy column for the energy selection (see also van der Heyden et al. (2002)).

3. Spectral Analysis Using Suzaku/XIS Data

3.1. Extraction of the Source Photons

Figure 1 shows a Suzaku/XIS image in the 0.2–0.7 keV band. The centered source is SNR N103B, and the extended source to the west is SNR RX J050736–6847 (Chu et al. 2000), as observed by ROSAT. According to Chu et al. (2000), the position and radius of RX J050736–6847 are $(\alpha, \delta) = (05:07:36, -68^\circ 47' 52'')$ and $\sim 5'$, respectively, corresponding to ~ 70 pc in the LMC at a distance of 48 kpc (Macri et al. 2006).

Table 1. Observation log for N103B.

	Suzaku	Chandra
Observation ID	100013010	1045
Observation mode	Full window, no burst, no SCI	FAINT
Exposure (ks)	33	41
Count rate (counts s ⁻¹)	FI: 2.1* BI: 3.7*	0.6*

* Count rates of FI- and BI-CCDs of N103B in the 0.3–10.0 keV and 0.55–10.0 keV bands within a circle of radius $\sim 4.3'$ after background subtraction, respectively.

* Total count rate within a circle of radius $3'$ after background subtraction.

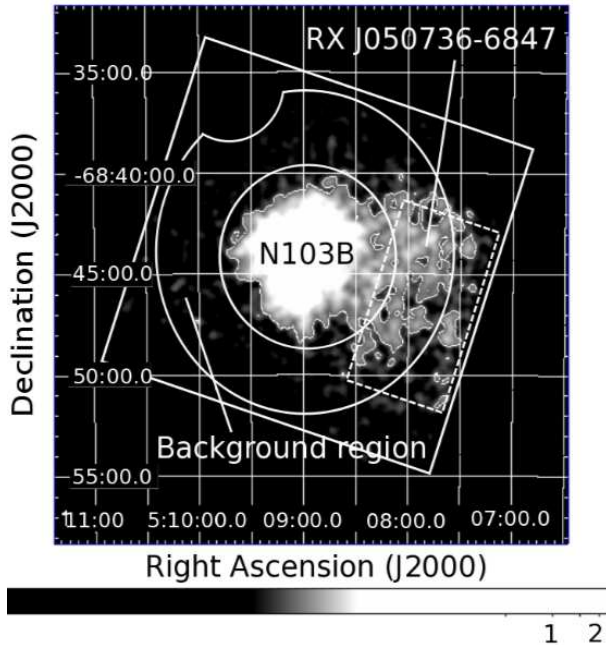


Fig. 1. Suzaku/XIS image of N103B in the 0.2–0.7 keV band. The images from all four XIS modules were combined. The white solid square shows the XIS field of view. The ^{55}Fe calibration sources in each XIS corner were masked. The image was smoothed using a Gaussian function with a standard deviation of $\sim 21''$. The coordinates are represented in the equatorial coordinate system for epoch 2000. The contour was overlaid with a level of 0.02 counts px^{-1} . The extended source to the west is a known SNR, RX J050736–6847 (Chu et al. 2000). The white solid circle and annulus represent the source and background regions of N103B, respectively, and the white dotted region is the source RX J050736–6847.

To extract the source photons for N103B, we selected a circular region with a radius of $\sim 4.3'$ around N103B as the source region, while an annular region with an outer radius of $\sim 7.8'$ around the source region was selected as the background region. The ^{55}Fe calibration sources in the corner of the each XIS were masked. Figure 1 shows that the X-ray emission from RX J050736–6847 contaminates both the source and background regions for N103B. We therefore selected a rectangular region ($\sim 5.7' \times 9.4'$) without the N103B source region to estimate the contamination from RX J050736–6847. For the background region of this estimation, we used the same annular region excluding the RX J050736–6847 source region. As a result, the background-subtracted count rates of FI- and BI-CCDs from RX J050736–6847.8 were roughly 0.02 and 0.06 counts s^{-1} in the 0.5–2.0 keV band, respectively. We therefore ignored the emission from RX J050736–6847.8 in the following spectral analysis since these count rates amount to only $\sim 1\%$ – 2% of those from N103B (see Table 1).

In the spectral analysis, we used XSPEC version 11.3.2.aj. The XIS response matrix files (RMFs) and auxiliary response files (ARFs) were prepared with XISRMFGEN version 2007-05-14 and XISSIMARFGEN version 2008-04-05, respectively. The prepared ARFs and RMFs were combined with ADDRMF and MARFRMF in the FTOOLS package.

3.2. Full-band Spectra

3.2.1. Spectral Model

Based on observations by XMM-Newton (van der Heyden et al. 2002) and Chandra (Lewis et al. 2003), the emission was found to be closely reproduced by the optically thin thermal emission model under non-equilibrium ionization. We therefore adopted a VNEI model in the XSPEC library (Hamilton et al. 1983, Borkowski et al. 1994, Liedahl et al. 1995, Borkowski et al. 2001). In the spectral analysis, we obtained the plasma temperature (kT_e), the metal abundance A_i (relative to the solar abundance), the ionization parameters $n_e t_{\text{ion}}$ (where n_e and t_{ion} are the plasma number density and the elapsed time of the shock, respectively), and a normalization $\frac{10^{-14}}{4\pi D^2} \int n_e n_H dV$ (where D , n_H , and dV are the distance to the source, the hydrogen number density, and the volume element of plasma, respectively). It should be noted that the VNEI code version 2.0 does not include K-shell emission lines for ions below the He-like state. We therefore

used VNEI code version 1.1, which in turn does not include the line emission from Ar., and we specifically added a GAUSSIAN model to the XSPEC library for the Ar He-like $K\alpha$ transition (~ 3.14 keV).

The average metal abundances in the LMC have been measured to be ~ -0.3 dex (Russell & Dopita 1992). We calculated the absolute abundances using the data presented by Russell & Dopita (1992). Since we used the abundance table from Anders & Grevesse (1989) in XSPEC, we compared the calculated abundances with those in Anders & Grevesse (1989) and derived the relative abundance for XSPEC. The best value in the second column of Table 2 shows the relative abundances used in this study. For Si, we used the value by Russell & Dopita (1992) (right column of Table 2). These values are consistent with those in other studies (Hughes et al. 1998; Keller & Wood 2006; Glatt et al. 2010).

Emission from sources in the LMC is attenuated through absorption by interstellar matter in both the Milky Way and the LMC. Since the metal abundances of these two absorption components are significantly different, we estimated the absorptions as follows. The abundances in absorbing matter in our Galaxy were assumed to be solar abundances (Anders & Grevesse 1989), and the hydrogen column density was denoted as $N_{\text{H}}^{\text{Galactic}}$. The value of $N_{\text{H}}^{\text{Galactic}}$ for N103B has already been determined to be $\sim 6.2 \times 10^{20}$ Hcm^{-2} in the Galactic HI survey (Dickey & Lockman 1990). We fixed $N_{\text{H}}^{\text{Galactic}}$ at this value and used the PHABS model in the XSPEC library. We also assumed that the absorbing matter in the LMC has the abundance pattern shown in Table 2. This absorption component is denoted as $N_{\text{H}}^{\text{LMC}}$, and we used the VPHABS model in the XSPEC library, and allowed the value to vary.

The calibration uncertainty of the normalization and the hydrogen column density for XIS 0, 1, 2, and 3 were estimated to be roughly $\sim 1\%$ – 10% and $(3.0\text{--}3.5) \times 10^{21}$ Hcm^2 , respectively, from the estimation of the systematic uncertainty for the Crab Nebula (Serlemitsos et al. 2007). We therefore allowed these parameters to fluctuate between FI and BI CCDs in the following spectral analysis. In addition, in the early phase of the Suzaku mission, the energy gain of XIS had an uncertainty of a few eV (Koyama et al. 2007). In previous studies on SNRs, the uncertainty was estimated to be ~ 10 eV at a maximum (see also Yamaguchi et al. (2008), Bamba et al. (2008), and Someya et al. (2010)). We used the range of 0.55–10.0 keV for FI and 0.3–10.0 keV for BI, and excluded data in the 1.7–1.8 keV band due to the uncertainty of XIS calibration around the Si-K edge (Koyama et al. 2007) in the spectral analysis.

The emission of SNRs is a mix of what is produced in different plasma components in the ejecta and the ISM. In some cases, especially for young SNRs, this is natural since both ISM and ejecta can be non-uniform, and the shock wave propagates with a long time scale to heat them up. Performing fitting with such a complex model is associated with considerable uncertainty in determining the parameters. Therefore, we began with a simple plasma

model and added more free parameters if necessary.

3.2.2. Models with One and Two Plasma Components

We began with the spectral analysis with models using 1 or 2 VNEI components attenuated by photoelectric absorption. The abundances of elements from C to Ni were set to vary in each plasma to maximize the degree of freedom. These models were unable to provide an acceptable fit. The $\chi^2/d.o.f.$ values for these models are summarized in Table 3 under (a) One-temperature plasma and (b) Two-temperature plasma.

3.2.3. Model with Three Plasma Components

In the previous section, we found that a reasonable fit of the emission requires at least three plasma components. We therefore adopted a third VNEI component. The European Photon Imaging Camera (EPIC) Metal-Oxide Semiconductor (MOS) and RGS onboard XMM-Newton observations (van der Heyden et al. 2002) have already demonstrated that we need at least three thermal components. To minimize the number of model parameters, we assumed that some plasma components have a common origin, and show a common abundance pattern. Thus, ISM should have abundance patterns similar to that of LMC, whereas the abundance would be greater for ejecta. We divided the fitting into 3 cases, namely (c) 3ISM or 3Ejecta, (d) 1ISM + 2Ejecta and (e) 2ISM + 1Ejecta, where ‘‘ISM’’ and ‘‘Ejecta’’ denote interstellar medium heated by the forward shock and ejecta heated by the reverse shock, respectively. From model (c), we assumed the metal abundances to be the same for all three VNEI components (since the abundances should be the same for all components if they have a common origin), and we set the abundances of elements from C to Ni to vary. Different kT_e and $n_e t_{\text{ion}}$ were assumed for these components. Although model (c) improved the fit, it was still unacceptable. The $\chi^2/d.o.f.$ value for this model is summarized in Table 3 under (c) 3ISM or 3Ejecta. For the three components in this model, the best-fit values for the temperature kT_e were estimated to be roughly ~ 0.22 , ~ 0.67 , and ~ 2.75 keV, and the ionization parameter $\log(n_e t [\text{cm}^{-3}\text{s}])$ was estimated to be ~ 13 , ~ 13 , and ~ 11 . In this regard, based on XMM-Newton EPIC MOS and RGS observations, there have been already reports on the temperature ($0.55_{-0.32}^{+0.05}$, 0.65 ± 0.05 , and 3.5 ± 0.5) and the ionization parameter ($10.36_{-0.06}^{+1.64}$, > 12.34 , and 10.72 ± 0.06) (van der Heyden et al. 2002). The values obtained from XMM-Newton observations roughly agree with the values obtained with model (c). According to van der Heyden et al. (2002), the abundance of Fe is distributed among two cool components and one hot component. We therefore decoupled the abundance of Fe and performed another fit, but this also failed to reproduce the spectra ($\chi^2/d.o.f. = 1257.519/464 (= 2.71)$). This discrepancy could be due to higher statistics but lower spectral resolution of our study since a grating spectrometer was used in the XMM-Newton observations.

With models (d) and (e), in order to reduce the degree of freedom of the model parameters, the heavy element abundances were assumed to be the same for the

Table 2. Metal abundances in the LMC and comparison with other observations.

Element	Russell & Dopita (1992)*	Hughes et al. (1998)*
O	0.26 (0.22–0.30)	0.19 (0.16–0.32)
Ne	0.33 (0.29–0.37)	0.29 (0.24–0.35)
Mg	0.78 (0.58–1.05)	0.32 (0.27–0.37)
Si	1.82 (highly uncertain)	0.31 (0.26–0.37)
S	0.31 (0.25–0.38)	0.36 (0.27–0.49)
Ca	0.34 (0.23–0.49)	-
Fe	0.36 (0.26–0.50)	0.22 (0.17–0.28)
Ni	0.62 (0.50–0.76)	-

*Si abundance is highly uncertain.

*Ca and Ni abundances have not been measured.

Table 3. Plasma models and their respective $\chi^2/d.o.f.$ values.

Model*	Plasma origin [†]	$\chi^2/d.o.f.$ ($=\chi^2_\nu$)
1 VNEI component	(a) One-temperature plasma	5102.99/471 (= 10.8)
2 VNEI components	(b) Two-temperature plasma	1424.11/458 (= 3.11)
3 VNEI components	(c) 3ISM or 3Ejecta	1267.236/465 (= 2.73)
3 VNEI components	(d) 1ISM + 2Ejecta	1062.649/463 (= 2.30)
3 VNEI components	(e) 2ISM + 1Ejecta	820.264/463 (= 1.77)
4 VNEI components	(f) 2ISM + 2Ejecta	795.709/460 (= 1.73)
4 VNEI components	(g) 3ISM + 1Ejecta	632.837/460 (= 1.38)
5 VNEI components	(h) 3ISM + 2Ejecta	626.858/457 (= 1.37)
5 VNEI components	(i) 4ISM + 1Ejecta	645.656/457 (= 1.38)

* Indicates the number of VNEI components.

[†] Model (a) assumes one-temperature ISM or ejecta, whereas model (b) assumes two-temperature ISM, two-temperature ejecta, or one-temperature ISM with one-temperature ejecta. In models (c) – (i), “ISM” and “Ejecta” indicate interstellar matter and ejecta components, respectively. The number x in x ISM and x Ejecta represents the number of components of the respective type. We took the metal abundance to be the same for all multi-temperature variable abundance non-equilibrium ionization (VNEI) components of the same plasma origin. For instance, the 1ISM + 2Ejecta model represents emission from one ISM component and two ejecta components. In the assumption of ISM and ejecta, the abundances, which could not be determined from spectral analysis, were fixed at the LMC average (Russell & Dopita 1992) and 1 solar, respectively.

two VNEI components of the same type (i.e., 2ISM and 2Ejecta). In the case of one ISM and two ejecta components, we were unable to obtain reasonable constraints for the abundances of He, C, N, S, Ca, and Ni through spectral analysis. We therefore fixed these parameters of the ISM component to the average values for LMC (He = 0.89, C = 0.30, N = 0.12, S = 0.31, Ca = 0.34, and Ni = 0.62 times solar). Furthermore, in the case of one ejecta and two ISM components, reasonable constraints could not be obtained for the abundances of He, C, N, and O of the ejecta component, and thus we fixed each of these abundances at 1 solar. Neither model was able to provide an acceptable fit, although the $\chi^2/d.o.f.$ values were significantly improved. The $\chi^2/d.o.f.$ values for these models are summarized in Table 3 under (d) 1ISM + 2Ejecta and (e) 2ISM + 1Ejecta.

3.2.4. Models with Four and Five Plasma Components

In the previous section, it was demonstrated that a reasonable fit of the emission requires yet another component. We therefore adopted a fourth thermal plasma component. Since model (e) 2ISM + 1Ejecta provided the best

fit, we added another VNEI component (ejecta in model (f) and ISM in model (g)) to model (e). The heavy element abundances were taken to be the same for both ISM and ejecta, and the free parameters were the same as those in the models presented in §3.2.3. Model (f) resulted in only slight improvement compared with model (e). In contrast, model (g) resulted in a significant improvement in the closeness of fitting. The $\chi^2/d.o.f.$ values for these models are summarized in Table 3 under (f) 2ISM + 2Ejecta and (g) 3ISM + 1Ejecta.

Finally, we added another VNEI component (ejecta in model (h) and ISM in model (i)) to model (g). However, in either case there was no significant improvement in fitting compared to model (g). The $\chi^2/d.o.f.$ values for these models are summarized in Table 3 under (h) 3ISM + 2Ejecta and (i) 4ISM + 1Ejecta.

We regarded model (g) as the best-fit spectral model. There are still residuals in the low energy end of the Fe-K line, which could not be closely reproduced by any of the multi-temperature VNEI plasma models. Thus, we added a GAUSSIAN in the XSPEC library.

We present the best-fit spectra and parameters in Figure 2 (a) and Table 4, respectively. The three ISM components are shown in green, blue, and orange, and the ejecta component is shown in cyan. The Gaussians (shown in magenta) represent the line emissions from Ar $K\alpha$ and Fe-K. The difference of best-fit values of $n_{\text{H}}^{\text{LMC}}$ and the normalization between FI and BI data were $\sim 0.4 \times 10^{21} \text{ Hcm}^2$ and $\sim 1\%$, and the best-fit gain offset values of FI and BI were $\pm 0.0 \text{ eV}$ and -8.0 eV , respectively. These values are within the calibration uncertainty. Note that the best-fit values did not change significantly upon fixing the energy gain to 0 and taking the same normalization and n_{H} for FI and BI.

3.2.5. Model with Four Plasma Components with Pure Metal Plasma Assumption

The spectral fitting in §3.2.4 requires a single ejecta component with abundances of ~ 0.06 –30 solar. The intensity of thermal bremsstrahlung (free-free emission) is proportional to $\sum_{i=\text{H}}^{i=\text{Ni}} n_e n_i Z_i^2$, where i , n_i , and Z_i represent an element, its number density, and the ion charge of element i , respectively. The species denoted by i are H, He, C, N, O, Ne, Mg, Si, S, Ca, Fe, and Ni in the VNEI plasma code version 1.1 in the XSPEC library. With the aid of the observed abundances (A_i), the solar abundances ($n_{i\odot}$) and the hydrogen number density (n_{H}), $\sum_{i=\text{H}}^{i=\text{Ni}} n_e n_i Z_i^2$ is $\sum_{i=\text{H}}^{i=\text{Ni}} A_i A_{i\odot} Z_i^2 n_e n_{\text{H}}$. If the plasma consists only of hydrogen, $\sum_{i=\text{H}}^{i=\text{Ni}} A_i A_{i\odot} Z_i^2 n_e n_{\text{H}}$ is $1 \times n_e n_{\text{H}}$. The plasma therefore consists mainly of hydrogen when the coefficient $A_i A_{i\odot} Z_i^2$ of $n_e n_{\text{H}}$ for elements from C to Ni is smaller than 1. Thus, the plasma assumed in §3.2.4 contains predominantly hydrogen (hence H-dominated plasma) since $A_i A_{i\odot} Z_i^2 < 0.5 \ll 1$ for elements from C to Ni. In contrast, when the plasma consists mainly of heavy elements, such as in the case of ejecta from the inner core of the progenitor star, $A_i A_{i\odot} Z_i^2$ for elements from C to Ni is considerably greater than 1, and we must apply special adjustments to the plasma model in performing fitting with the XSPEC package. Here, we assumed that the plasma consisted of heavy elements from C to Ni with $A_i A_{i\odot} Z_i^2 \gg 1$ (pure metal plasma) and examined which plasma model is more suitable in the case of N103B. Pure metal plasma has also been discussed in Vink et al. (1996), Yamaguchi et al. (2008), and Kosenko et al. (2010). In these studies, they derived that the abundance of heavy elements are in the order of 10^4 .

In the previous section, the 3ISM + 1Ejecta model produced the best fit. In this model, the single ejecta component clearly corresponds to ejecta with abundances of ~ 0.06 –30 solar. We therefore fixed the abundances of elements from C to O for the ejecta at 10^4 solar in order to model plasma poor in hydrogen and rich in heavy elements, and fitted the spectra again. This is the same method shown in Yamaguchi et al. (2008) and Vink et al. (1996).

The abundance of elements from C to O can take any value much greater than 1 (i.e., $A_i A_{i\odot} Z_i^2 \gg 1$); for instance, the abundances of elements from C to O can be fixed at 10^5 or even 10^6 solar. Thus, the values of $A_i A_{i\odot} Z_i^2$

for elements from C to O satisfy the assumption of pure metal plasma. The spectra reproduce a unique solution to obtain convergence to a constant value of the product of the abundance of elements from C to Ni and the normalization ($A_i \times \text{Norm} = \text{const}$). Because of this, we fixed these abundances at $\sim 10^5$ – 10^6 solar to estimate the statistical error of the emission measure. For these abundances, we also fixed the emission measure at $2.74 \times 10^{55} \text{ cm}^3$. The absolute values of these abundances and the emission measure obtained by the spectral analysis do not play an important role. This method is commonly used for reproducing pure-metal plasma in the XSPEC package (Yamaguchi et al. 2008).

Table 5 and Figure 2 (b) show the best-fit parameters and spectra, respectively. The fitting shows a reduced χ^2 similar to that in the H-dominant plasma model. Note that whereas the high-energy continuum in the 4.0–6.0 keV band corresponds to ejecta in the H-dominant plasma model, it corresponds to the high-temperature ISM component in the pure metal plasma model, and the Fe-K line is from an ejecta component in both models.

3.3. Spectral Analysis Around Fe-K Line

In the previous section, we showed that the emission was closely reproduced with four plasma components, but still had residuals at the low-energy end of the Fe-K line. This implies that the plasma emitting the Fe-K line has a relatively low degree of ionization. We therefore fitted the spectrum in the 4.0–10.0 keV band using a plane-parallel non-equilibrium ionization VPSHOCK model in XSPEC, which integrates the emission with ionization parameters varying linearly from 0 to $n_e t_{\text{ion}}$ (see also Hughes et al. (2000)).

In the spectral analysis, we fixed the temperature at the best-fit value of 3.96 keV (see Table 4). We fitted the spectrum by taking the normalization and $n_e t_{\text{ion}}$ as variables. As a result, the fit was accepted with $\chi^2/d.o.f.$ of 18.46/39 (= 0.43). The best-fit values of the ionization parameter, the emission measure, and the abundance of Fe were estimated to be 10.81 (10.73–10.89), 0.39 (0.35–0.43) $\times 10^{59} \text{ cm}^{-3}$, and 4.74 (3.71–5.96) solar, respectively. These best-fit values were close to the values obtained with the H-dominated plasma model. Figure 3 shows the best-fit spectra, where the fit of the residual at the low-energy end of Fe-K was clearly improved with the VPSHOCK model.

4. Image Analysis Using Chandra/ACIS Data

In this section, we analyzed images obtained with Chandra/ACIS to reveal the distribution of heavy elements from O to Fe-K heated by the forward and reverse shocks. In the first step in studying the distribution, we prepared continuum-subtracted images (CS images) for elements from Si to Fe-K in the same way as in Hwang et al. (2000) and Lewis et al. (2003). Below, we briefly describe the procedure for preparing CS images. More detailed explanations are presented in Hwang et al. (2000) and Lewis et al. (2003).

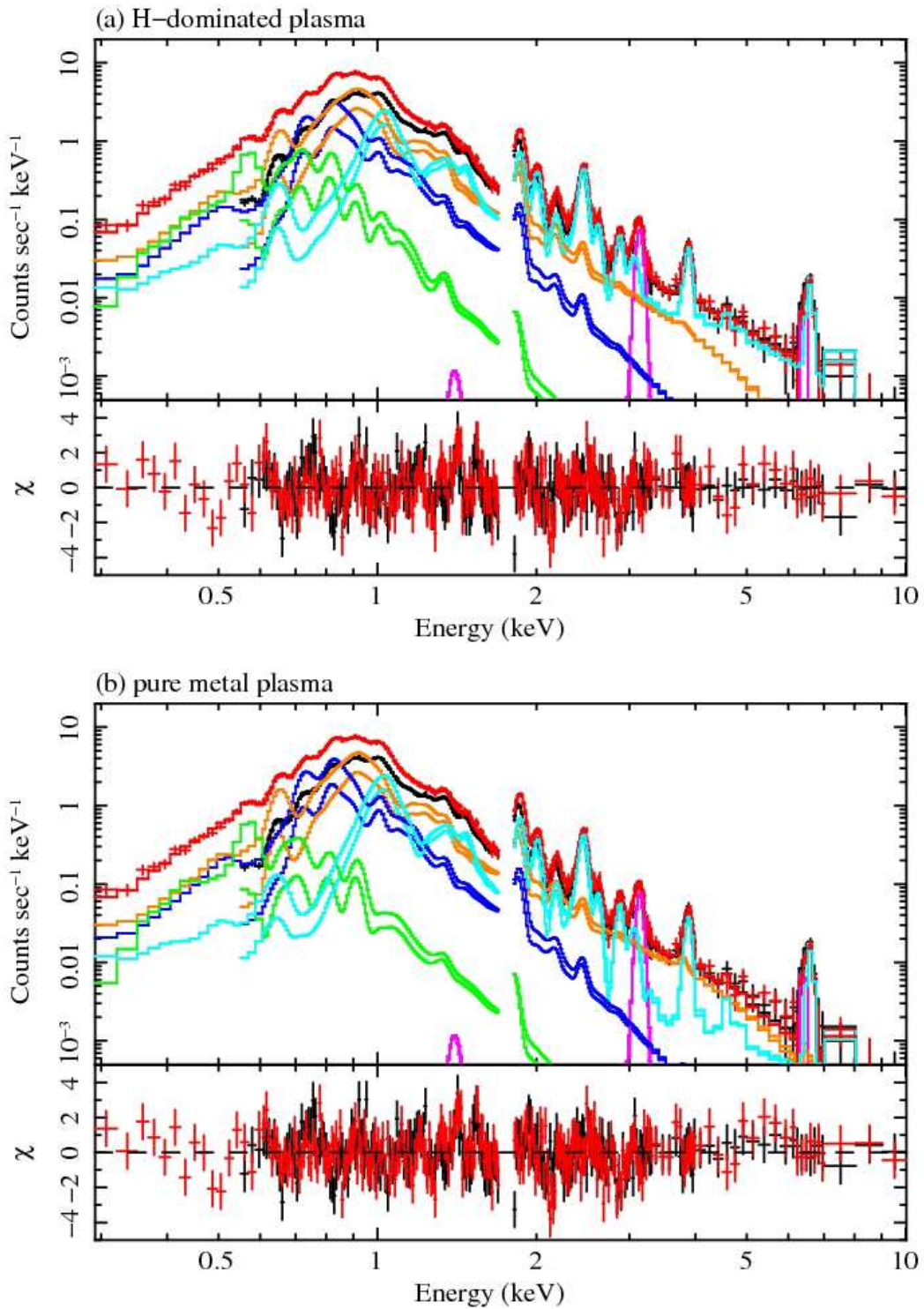


Fig. 2. (a) : H-dominated plasma model. (b): Pure metal plasma model. Upper panels: background-subtracted XIS spectra in the 0.3-10.0 keV band. The black and red data points represent the FI and BI spectra, respectively. The three ISM components are shown in green, blue and orange, and the ejecta component is shown in cyan. The Gaussians (shown in magenta) represent the lines for Ar K α and Fe K, respectively. Lower panels: residuals from the best-fit model. Data in red and black represent FI and BI, respectively.

Table 4. Best-fit parameters for N103B modeled with H-dominated plasma*.

Parameter	ABSORPTION COMPONENTS			
$N_{\text{H}}^{\text{Galactic}}$ ($\times 10^{20}$ cm $^{-2}$)	6.2 (fixed)			
$N_{\text{H}}^{\text{LMC(FI)}}$ ($\times 10^{21}$ cm $^{-2}$)	2.97 \pm 0.06			
$N_{\text{H}}^{\text{LMC(BI)}}$ ($\times 10^{21}$ cm $^{-2}$)	2.55 $^{+0.04}_{-0.03}$			
Parameter	PLASMA COMPONENTS			Ejecta component
Parameter	ISM components			Ejecta component
kT_{e} (keV)	0.319 $^{+0.007}_{-0.005}$	0.547 $^{+0.005}_{-0.006}$	0.962 \pm 0.005	3.96 \pm 0.01
$\log(n_{\text{e}}t)$ (cm $^{-3}$ s)	10.48 $^{+0.05}_{-0.08}$	>11.88	10.89 \pm 0.01	10.795 $^{+0.007}_{-0.006}$
EM^{\dagger}	1.17 $^{+0.97}_{-0.06}$	2.33 $^{+0.04}_{-0.05}$	2.60 \pm 0.04	0.197 $^{+0.003}_{-0.001}$
H ‡	1.00 (fixed)			1.00 (fixed)
He	0.89 (fixed)			1.00 (fixed)
C	0.30 (fixed)			1.00 (fixed)
N	0.12 (fixed)			1.00 (fixed)
O	0.153 $^{+0.006}_{-0.005}$			1.00 (fixed)
Ne	0.180 $^{+0.002}_{-0.004}$			<0.06
Mg	0.134 $^{+0.011}_{-0.010}$			2.27 \pm 0.17
Si	0.63 $^{+0.03}_{-0.02}$			9.7 \pm 0.3
S	0.31 (fixed)			17.2 $^{+0.5}_{-0.4}$
Ca	0.34 (fixed)			30 \pm 3
Fe	0.523 $^{+0.005}_{-0.006}$			4.19 $^{+0.07}_{-0.09}$
Ni	0.62 (fixed)			18.6 $^{+1.8}_{-1.6}$
Line	Center energy (keV)		Normalization (photons cm $^{-1}$ s $^{-1}$)	
Ar He-like K α	3.141 \pm 0.005		3.8 $^{+0.3}_{-0.4}$ $\times 10^{-5}$	
Fe-K	6.43 $^{+0.02}_{-0.03}$		6.8 $^{+1.7}_{-2.2}$ $\times 10^{-6}$	
Const (FI)	1.00 (fixed)			
Const (BI)	1.000 $^{+0.007}_{-0.004}$			
FI gain offset (eV)	-7.475 \pm 0.005			
BI gain offset (eV)	-0.2 $^{+0.2}_{-0.8}$			
$\chi^2/d.o.f.$	602.272 / 458 (= 1.32)			

* Errors represent 90% confidence intervals.

\dagger Emission measure $EM = \int n_{\text{e}}n_{\text{H}}dV = n_{\text{e}}n_{\text{H}}V$ in units of 10^{59} cm $^{-3}$. The distance to N103B was assumed to be 48 kpc (Macri et al. 2006).

\ddagger Abundance is relative to the solar abundance (Anders & Grevesse 1989), and a common value is assumed for all three ISM components.

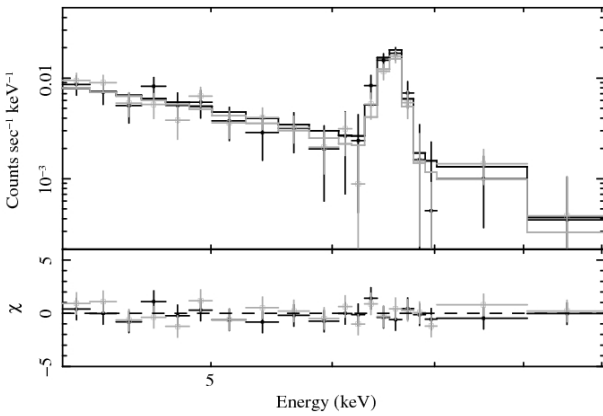


Fig. 3. Upper panel: Background-subtracted XIS spectra in the 4.0–10.0 keV band. Lower panel: Residuals from the best-fit models. In both panels, data in black and light gray represent the FI and BI spectra, respectively.

First, we produced raw line energy band images (I_{L}) and continuum energy band images (I_{C}) for each element. The energy intervals for I_{L} and I_{C} are summarized in the second and third columns in Table 6 and the horizontal bars above and below in the spectrum of Figure 4, respectively. We selected the energy band of I_{C} to be as close as possible to that of I_{L} , to avoid line features. The same continuum component as for Ca was also used for Ar to avoid the line emission from Ca He β (\sim 4.58 keV).

In the next step, using spectral analysis, we estimated the continuum flux (F_{C}^*) included in I_{L} . We extracted the spectrum of the entire remnant and obtained the response matrix using the SPEXTRACT command in CIAO version 4.1.2. The spectra were fitted with a POWER LAW for the continuum emission and GAUSSIANS for line emissions in the XSPEC library in the 1.5–10.0 keV band. Figure 4 shows the best-fit background-subtracted spectrum. The best-fit value for the photon index and the normalizations are summarized in Table 6. The fluxes included in I_{L}

Table 5. Best-fit parameters for N103B modeled with pure metal plasma*.

Parameter		ABSORPTION COMPONENTS		
$N_{\text{H}}^{\text{Galactic}} (\times 10^{20} \text{ cm}^{-2})$		6.2 (fixed)		
$N_{\text{H}}^{\text{LMC(FI)}} (\times 10^{21} \text{ cm}^{-2})$		$3.07^{+0.04}_{-0.10}$		
$N_{\text{H}}^{\text{LMC(BI)}} (\times 10^{21} \text{ cm}^{-2})$		$2.74^{+0.05}_{-0.11}$		
Parameter		PLASMA COMPONENTS		
		ISM components		Ejecta component
KT_e (keV)	$0.328^{+0.001}_{-0.013}$	$0.522^{+0.01}_{-0.001}$	$1.29^{+0.01}_{-0.02}$	$4.01^{+0.05}_{-0.08}$
$\log(n_e t)$ (cm^{-3}s)	$10.11^{+0.08}_{-0.09}$	>11.86	$10.654^{+0.006}_{-0.005}$	$10.785^{+0.005}_{-0.008}$
EM^\dagger	$8.55^{+0.66}_{-1.10}$	$23.9^{+0.9}_{-1.1}$	17.3 ± 0.7	$2.74^{+0.11}_{-0.04} \times 10^{-5}$
H^\ddagger		1.00 (fixed)		1.00 (fixed)
He		0.89 (fixed)		1.00 (fixed)
C		0.30 (fixed)		1.00×10^4 (fixed)
N		0.12 (fixed)		1.00×10^4 (fixed)
O		$0.131^{+0.005}_{-0.006}$		1.00×10^4 (fixed)
Ne		$0.18^{+0.01}_{-0.02}$		$< 2.6 \times 10^4$
Mg		0.11 ± 0.1		$1.3^{+0.3}_{-0.1} \times 10^5$
Si		$0.55^{+0.03}_{-0.02}$		$5.6^{+0.1}_{-0.2} \times 10^5$
S		0.31 (fixed)		$9.9 \pm 0.3 \times 10^5$
Ca		0.34 (fixed)		$1.7 \pm 0.1 \times 10^6$
Fe		$0.512^{+0.005}_{-0.004}$		$2.46^{+0.06}_{-0.05} \times 10^5$
Ni		0.62 (fixed)		$8.6^{+1.3}_{-0.6} \times 10^5$
Line		Center energy (keV)		Normalization (photons $\text{cm}^{-1} \text{s}^{-1}$)
Ar He-like $K\alpha$		3.141 ± 0.007		$(3.7 \pm 0.5) \times 10^{-5}$
Fe-K		6.43 ± 0.04		$7.0 \pm 3.0 \times 10^{-6}$
Const (FI)		1.00 (fixed)		
Const (BI)		1.008 ± 0.01		
FI gain offset (eV)		-7.2 ± 0.1		
BI gain offset (eV)		$-0.5^{+0.4}_{-0.5}$		
$\chi^2/d.o.f.$		644.936 / 458 (= 1.41)		

* Errors represent 90% confidence intervals. In the estimation of the statistical error of the normalization, we fixed the abundance at $\sim 10^5$ – 10^6 solar. In the estimation of the statistical error of the abundance, we fixed the emission measure.

† Emission measure $EM = \int n_e n_H dV = n_e n_H V$ in units of 10^{57} cm^{-3} . The distance to N103B was assumed to be 48 kpc (Macri et al. 2006).

‡ Abundance is relative to the solar abundance (Anders & Grevesse 1989), and a common value is assumed for all three ISM components.

Table 6. Information necessary for preparing continuum-subtracted images.

CONTINUUM COMPONENT*					
Photon index = 3.7 ± 0.1 , Normalization = $5.4^{+0.6}_{-0.5} (\times 10^{-3} \text{ photons keV}^{-1} \text{ cm}^{-2} \text{ s}^{-1})$					
INFORMATION NECESSARY FOR PREPARING CONTINUUM-SUBTRACTED IMAGES					
Element	Line (I_L) (eV)	Continuum (I_C) (eV)	Flux (F_C^*) ($\times 10^{-5} \text{ photons cm}^{-2} \text{ s}^{-1}$)	Flux (F_C) ($\times 10^{-5} \text{ photons cm}^{-2} \text{ s}^{-1}$)	$R = \frac{F_C^*}{F_C}$
Si	1750–1915	1560–1735	9.19	14.60	0.63
S	2340–2540	2625–2825	3.78	2.49	1.52
Ar	3025–3225	3350–3550	1.48	1.02	0.15
Ca	3750–3950	3350–3550	0.68	1.02	0.66
Fe	6200–6800	5400–6000	0.28	0.46	0.61

* Errors represent 90% confidence intervals.

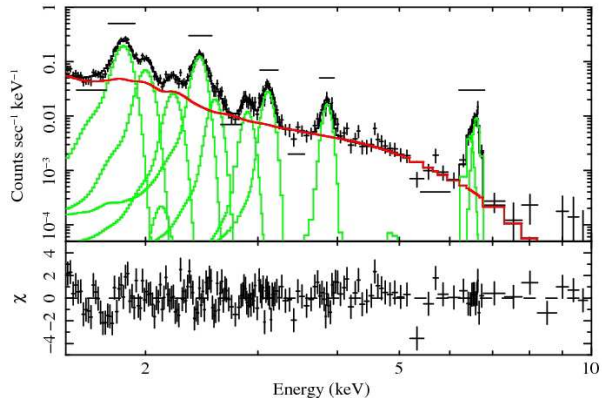


Fig. 4. Background-subtracted Chandra/ACIS spectrum of N103B. The horizontal bars above and below the spectrum show the energy interval for line and continuum images used for preparing continuum-subtracted images (see text).

($= F_C^*$) and I_C ($= F_C$) are summarized in the fourth and fifth columns in Table 6.

A continuum image (I_C^*) included in the energy band of I_L can be obtained from $R \times I_C$, where R is $\frac{F_C^*}{F_C}$. Thus, the pure line image is given by $I_L - I_C^*$. Figure 5 shows the pure line images for Si, S, Ar, Ca, and Fe-K.

Regarding the pure line images for O and Fe-L, we were unable to prepare CS images since it was rather difficult to estimate I_C for O and Fe-L with the Chandra spectral resolution. We therefore prepared only energy-selected images at 0.5–0.7 keV for O and 0.7–0.8 keV for Fe-L (Figure 5). We also prepared low-energy band image in the 0.5–0.9 keV and high-energy continuum image in the 5.2–6.0 keV band (Figure 5).

5. Discussion

5.1. Complex Emission Features

In this section, we discuss the complex emission features based on spectral and image analysis.

5.1.1. Emission Origin

In § 3, we found that the plasma emission from N103B can be closely reproduced by three ISM components and one ejecta component. In this section, we discuss the plasma origin.

The elemental abundances reflect the plasma in the environment and the progenitor of the SNR. In Tables 4 and 5, the abundances for the three ISM components are significantly lower than the solar abundances, and roughly consistent with the LMC average up to a factor of 2, whereas the abundances for the ejecta component are notably higher than the solar abundances. These results provide clues regarding the emission origin, suggesting that the three ISM and one ejecta components are emitted from ISM heated by the forward shock and ejecta heated by the reverse shock, respectively. Each ISM plasma component has different values of kT and $n_e t$. This might be due to the different time scales of heating by the forward shock. The middle-temperature component has a large $n_e t$, which

suggests that it may have been heated immediately after the supernova explosion or represents the emission of the dense gas in the ISM. In contrast, the hot and cool components have smaller $n_e t$. Their respective emission measures are similar to that of the middle-temperature component, and thus it is not due to a difference in density but a difference in time scale. These two components may have been heated recently. In order to discuss the origins of these three components further, we would need further CO and/or OH-maser observations to distinguish their spatial distributions.

5.1.2. Emission Morphology

Here, we discuss the spatial distribution of elements with a combination of spatial and spectral analysis. The ejecta component has already been identified with ejecta heated by the reverse shock. Specifically, the spectral analysis suggests that the Fe-K emission in Figure 5 corresponds to ejecta (Figure 2). Thus, the Fe-K image provides a good indication of the distribution of the X-ray emitting ejecta. The line emissions for elements from Si to Ca also correspond to ejecta based on the spectral analysis, although there is also Si emission from ISM. In Figure 5, the bright spots in the images for elements from Si to Ca are located to the southwest, which is rather similar to the case of Fe-K. This morphology supports our interpretation about the ejecta emission. In contrast, in Figure 5 the Fe-K emission is located slightly inward compared with the emissions of lighter elements. The layered structure of ejecta could be preserved after a supernova explosion. Similar ejecta distributions have also been reported for the Tycho SNR observed with Suzaku/XIS based on its Doppler motion (Hayato et al. 2010).

In the ISM O and Fe-L emission images in Figure 5, it appears as though they do not overlap with the ejecta emission. This morphology also supports our interpretation about ISM emission. The 0.5–0.9 keV band image support it again. In addition, the ISM temperatures of ~ 0.32 , ~ 0.55 , and ~ 0.96 keV are significantly lower than the ejecta temperature of ~ 3.96 keV. These results indicate that the ejecta and ISM components are not dynamically connected (see also van der Heyden et al. (2002)). This result supports our discussion in § 5.1.1.

Figure 6 shows a Chandra/ACIS image in the 5.2–6.0 keV band. The overlapping contours represent O (magenta), Fe-L (green), and Fe-K (cyan), respectively. The high-energy continuum is located away from the ISM component represented by O and Fe-L, and corresponds to the bright spot for Fe-K, suggesting that the origin of the high-energy continuum is the ejecta.

5.2. Discussion on Progenitor of N103B

In this section, we discuss the progenitor of N103B. In many cases, it is difficult to determine whether the progenitor is of Type Ia or II. Although the detection of a light echo spectrum and the presence of a pulsar are powerful tools for determining the progenitor type, in many cases we have to rely on abundance patterns, heavy element masses, and/or the surrounding environment to determine the progenitor type. We discuss on the progenitor

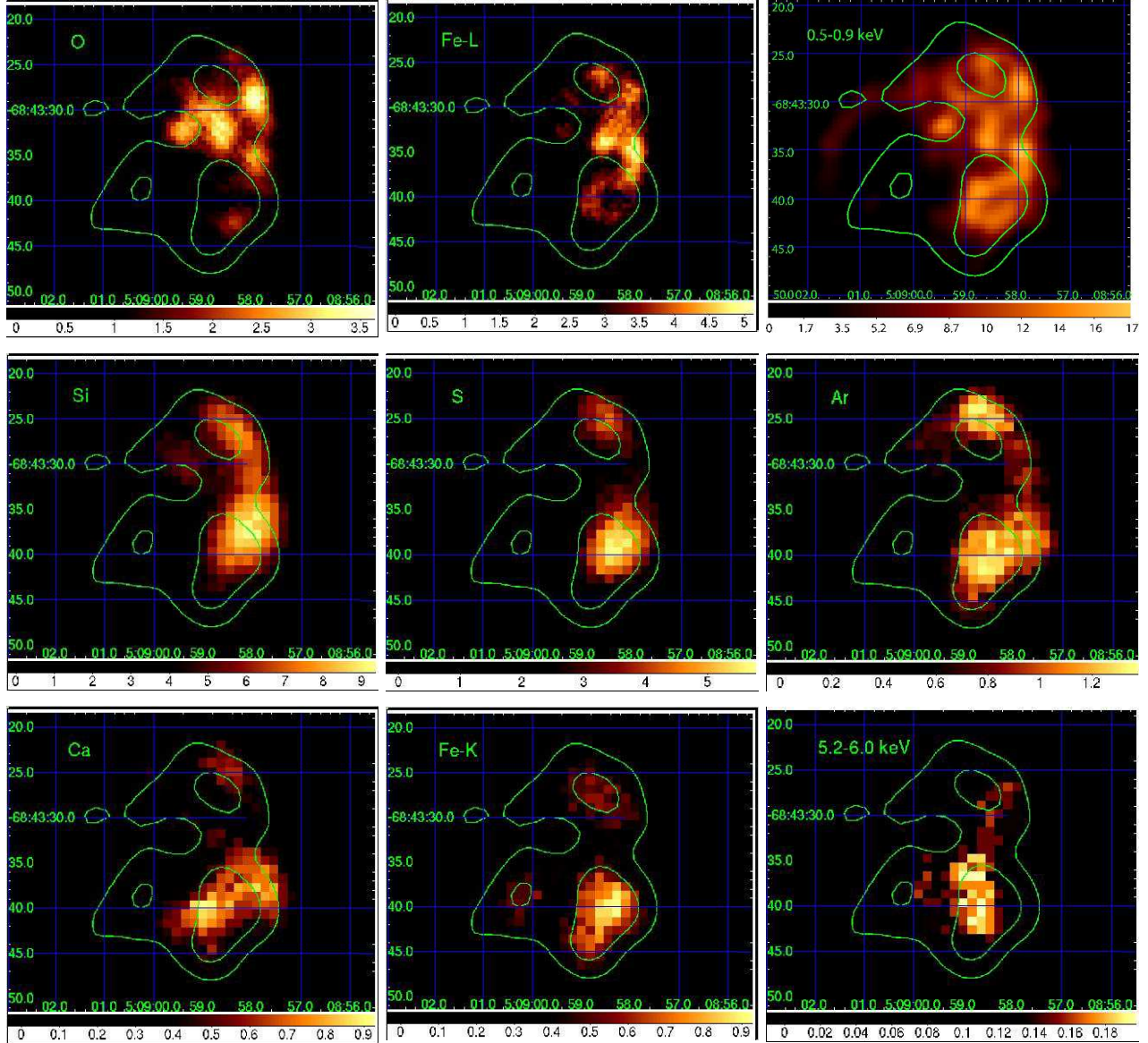


Fig. 5. Chandra/ACIS narrow-band images of N103B. The images labeled O and Fe-L are for O (0.5–0.7 keV) and Fe-L complex (0.7–0.8 keV) band images. These images are not smoothed. The image labeled 0.5–0.9 keV corresponds to the low-energy band image in the 0.5–0.9 keV. The images labeled Si, S, Ar, Ca, and Fe-K are continuum-subtracted images. Each image is smoothed using a top-hat function with $\sigma = 3$, and a bin size of $1''$. The image labeled 5.2–6.0 keV corresponds to the high-energy continuum in the 5.2–6.0 keV band. This image is smoothed using a top-hat function with $\sigma = 5$, and a bin size of $2.5''$. The overlapping contours represent 0.2 and 0.4 counts px^{-1} of the Fe-K line. The coordinates are in the equatorial coordinate system for epoch 2000.

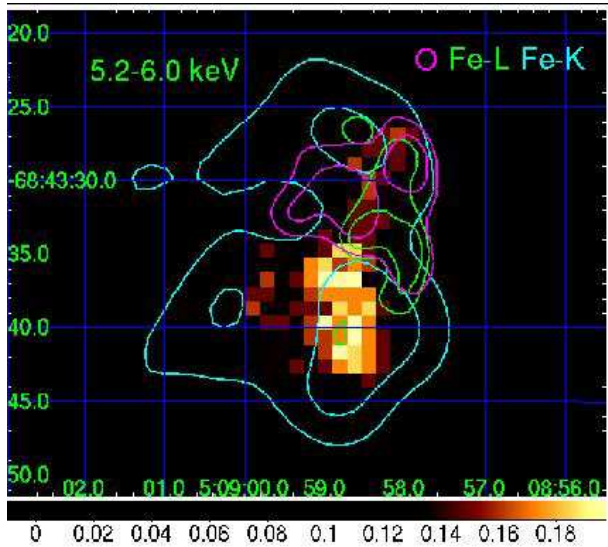


Fig. 6. Chandra/ACIS image of N103B in the 5.2–6.0 keV band. The image is smoothed with a tophat function with $\sigma = 5$, and a bin size of $2.5''$. The overlapping contours represent 1.7 and 2.3 counts px^{-1} for O, 3.5 (magenta), 4.0 counts px^{-1} for Fe-L (green), and 0.2 and 0.4 counts px^{-1} for Fe-K (cyan). The coordinates are in the equatorial coordinate system for epoch 2000.

of N103B with the spectral and imaging analysis results.

5.2.1. Progenitor Type

The supernova explosion type is essentially classified by the early-time spectra through optical observation. Based on the optical spectra, Type I and Type II are defined by the lack and presence of hydrogen structures, respectively (Filippenko 1997). These spectral features reflect the envelope of the star before the supernova explosion. In essence, optical observations should indicate whether the ejecta are composed of little hydrogen and a lot of metal (Type I) or a lot of hydrogen and little metal (Type II). These two types of ejecta are referred to as pure metal plasma and H-dominated plasma, respectively.

Figure 2 shows the best-fit spectra assuming (a) H-dominated plasma and (b) pure metal plasma. We can see that the origin of the 5–6 keV band continuum is different depending on the plasma type, where the origin is the ejecta for the H-dominated plasma model and the high-temperature ISM component in the pure metal plasma model. However, we cannot determine which model is correct on the basis of spectral analysis alone since the confidence intervals for the two models are comparable. We therefore utilize Chandra/ACIS images to determine the correct model. The spatial distribution of the high-energy continuum most likely corresponds to ejecta since it is similar to a distribution for ejecta. Combining spectral analysis based on Suzaku/XIS data with image analysis based on Chandra/ACIS data, we concluded that the progenitor of this remnant consisted of H-dominated plasma, in other words, it was a Type II progenitor.

A recent study (Lopez et al. 2011) favors a Type Ia progenitor for N103B. However, our results reveal some un-

certainty in that study. For example, Lopez et al. (2011) reported that the progenitor might be Type Ia on the basis of statistical image analysis of the morphologies from Si XIII and 0.5–2.1 keV emissions. However, applying that method to the present sample might be problematic since the Si XIII and 0.5–2.1 keV emissions are a combination of emissions from ISM and ejecta. The fact that N103B is associated with recent star formation (Badenes et al. 2009) may make it difficult to determine the progenitor type of N103B, and thus further studies are needed in order to reach an unambiguous conclusion.

With our new method, we can determine the progenitor type by using only observational data, without the need for a nucleosynthesis model. This method can help to distinguish between pure metal plasma (Type I) and H-dominated plasma (Type II) on the basis of detailed X-ray observations. The advantage of this method is the lower uncertainty compared with other methods (e.g., using plasma volume and a nucleosynthesis model). However, the disadvantages of this method are that it fails to distinguish between the Type Ia and Type Ib/c subclasses Type I and that it cannot provide an estimate of the progenitor mass. To obtain this information, we have to rely on other well-known methods.

5.2.2. Heavy Element Masses and Abundance Patterns

In the previous section, we showed that the progenitor was most likely Type II although there is still some uncertainty. Here, we estimate the progenitor mass by comparing the results of a nucleosynthesis model with observational data under the assumption that N103B has a Type II progenitor.

To calculate the hydrogen number density, we need to know the ejecta volume heated by the reverse shock. We therefore assumed a sphere with a radius of $\sim 4'' \simeq 0.93$ pc for the ejecta volume (V_{ejecta}), which was estimated from the southwest Fe-K knot shown in Figure 5. From this, V_{ejecta} was estimated to be $\sim 9.9 \times 10^{55} \text{ cm}^{-3}$ on the assumption that the plasma was contained in the uniform sphere and not in the shell. With the aid of the observed emission measure ($1.97_{-0.01}^{+0.03} \times 10^{58} \text{ cm}^{-3}$), V_{ejecta} and the volume filling factor (f), we calculated n_{H} by taking into account $n_{\text{e}} = 1.2n_{\text{H}}$ for fully ionized solar abundance plasma (Anders & Grevesse 1989) since the ejecta were reproduced by the H-dominated plasma model. In this case, n_{H} was estimated to be $\sim 12.87_{-0.03}^{+0.10} f^{-0.5} \text{ cm}^{-3}$.

The number density of heavy element i (n_i) is given by

$$n_i = A_{i\odot} A_i n_{\text{H}}, \quad (1)$$

where $A_{i\odot}$ and A_i are the solar abundance (Anders & Grevesse 1989) and the observed abundance relative to the solar abundance, respectively. We assumed that the proton mass (m_p) is equal to the neutron mass, and the electron mass was ignored. Then, the mass of heavy element i (M_i) is given by

$$M_i = \eta_i m_p n_i V_i, \quad (2)$$

where η_i and V_i are the mass number and ejecta volume of heavy element i , respectively.

We assumed that V_i for each element was equal to

V_{ejecta} , since the images for elements from Si to Fe-K were similar to that of Fe-K (Figure 5). We also assumed that V_i for Ne and Mg was equal to V_{ejecta} , although it is difficult to estimate V_i for Ne and Mg due to the ISM emission. Then, combining Equations 1 and 2, we can obtain the heavy element masses.

The obtained number density and mass of each element are listed in Table 7. For comparison, we also listed the heavy element masses calculated with the nucleosynthesis model for $13 M_{\odot}$ (Nomoto et al. 1997) and Type Ia W7 (Iwamoto et al. 1999), respectively. The isotope masses calculated from the nucleosynthesis model for the same element were summed. The observed masses were significantly lower compared to those calculated with the nucleosynthesis model. The ejecta morphology has a strongly asymmetric nature, and it appears that the eastern part of N103B may start to be heated only recently by the reverse shock because of non-uniform surrounding matter and/or asymmetric explosion. If the ejecta is not uniformly heated, the observed mass is lower than that calculated with the nucleosynthesis model. van der Heyden et al. (2002) reported the masses of Si and Fe to be 0.032 and $0.033 M_{\odot}$, respectively. These heavy element masses are close to the observed values, with a deviation of up to a factor of 3.

We estimated the progenitor mass by comparing the abundance pattern calculated with the nucleosynthesis model with that obtained from spectral analysis. With Equations 1 and 2, the abundance pattern calculated with the nucleosynthesis model relative to the solar abundance of elements i and j ($\equiv \frac{A_i}{A_j}$) is given by

$$\frac{A_i}{A_j} = \frac{\frac{n_i}{n_{\text{H}} A_{i\odot}}}{\frac{n_j}{n_{\text{H}} A_{j\odot}}} = \frac{n_i A_{j\odot}}{n_j A_{i\odot}} = \frac{\frac{M_i}{\eta_i m_{\text{p}} V_i} A_{j\odot}}{\frac{M_j}{\eta_j m_{\text{p}} V_j} A_{i\odot}} = \frac{\eta_j M_i V_j A_{j\odot}}{\eta_i M_j V_i A_{i\odot}}. \quad (3)$$

To calculate the abundance pattern, the isotope masses of each element were summed, and the averaged isotope mass was used as the mass number.

Assuming that heavy elements i and j have the same volume, the abundance pattern can be calculated from Equation 3. The data points plotted in cyan in Figure 7 represent the abundance pattern relative to that of Si and the solar abundance. For comparison, we also plotted the ratio predicted from the nucleosynthesis models for $13 M_{\odot}$ (black), $15 M_{\odot}$ (red), $20 M_{\odot}$ (green), and $25 M_{\odot}$ (blue) (Nomoto et al. 1997) and Type Ia W7 (cyan) (Iwamoto et al. 1999). Our results show that

As shown in Figure 7, the relative abundance of Mg is lower than Si, indicating the progenitor is a rather low-mass star. Fe and Ni abundance is rather high, which also indicates the low-mass progenitor. With these results, we estimated the progenitor mass as $13 M_{\odot}$. Note that the volume of Mg and Ni ejecta can be different from those of other elements, such as Si and Fe. $\frac{\text{Mg}}{\text{Si}}$ and $\frac{\text{Ni}}{\text{Si}}$ are therefore associated with a large uncertainty.

5.3. Propagation of Reverse Shock in Iron-rich Ejecta

In §3.3, we showed that the plasma emitting the Fe-K line has a relatively low degree of ionization compared

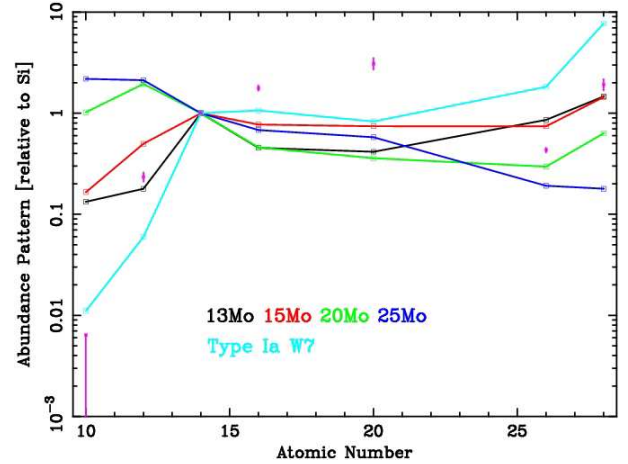


Fig. 7. Atomic number plotted against the calculated and observed abundance patterns relative to Si and the solar abundance. Black, red, green, and blue points represent the abundance patterns for 13, 15, 20, and 25 M_{\odot} assuming a CC progenitor (Nomoto et al. 1997). The cyan points represent the results for Type Ia W7 (Iwamoto et al. 1999). The purple data points represent the observed abundances pattern.

with plasma showing emission from other elements. A similar result is also reported in van der Heyden et al. (2002). Fe-K line emission originates from ejecta heated by the reverse shock, and thus the reverse shock might be propagating in Fe-rich ejecta at present.

5.4. Density, Total Energy, Swept-up Mass, and Age

Owing to the successful separation of the three ISM components from the single ejecta component, we can estimate the environment around N103B. In this section, we estimate the pre-shock (n_0) and post-shock (n_e) number density, the thermal energy (E_t), the swept-up mass (M_{swept}), and the ionization age of plasma (t_{ion}) to gain insight into the surrounding environment and the plasma nature for this remnant.

With the aid of the emission measure obtained from the spectral analysis, the volume of the plasma (V), and the volume filling factor (f), we calculated n_e by considering $n_e = 1.2n_{\text{H}}$ for fully ionized solar abundance plasma (Anders & Grevesse 1989). Under the assumption of strong shock and ideal gas, the pre-shock number density is obtained from $n_0 = \frac{n_{\text{H}}}{4}$ (known as the Rankine-Hugoniot relation), although recent studies on efficient cosmic ray acceleration in the SNR shocks have demonstrated that a higher compression ratio is required (e.g., Bamba et al. (2005)). The swept-up mass is given by $M_{\text{swept}} = n_{\text{H}} m_{\text{p}} V f$, and the total thermal energy is given by $E_t = 3n_e k T_e V f$, where k and T_e are the Boltzmann constant and the absolute temperature of the plasma, respectively. Electrons and ions are assumed to be in thermal equilibrium. The ionization age of plasma is calculated from n_e and $n_e t_{\text{ion}}$ obtained in the spectral analysis.

In order to estimate the plasma number density, we need to know the volume of the plasma, which can be derived from X-ray images. In § 5.1.2, we have already

Table 7. Number densities and masses of heavy elements.

Element	n_i (10^{-3} cm^{-3})	M_i ($10^{-3} M_\odot$)	13 M_\odot	W7
Ne	$< 0.1 f^{-0.5}$	$< 0.2 f^{+0.5}$	22	4.5
Mg	1.1 (1.0–1.2) $f^{-0.5}$	2.2 (2.0–2.4) $f^{+0.5}$	12	8.6
Si	4.4 (4.3–4.6) $f^{-0.5}$	10.3 (10.0–10.7) $f^{+0.5}$	70	157
S	3.6 (3.5–3.7) $f^{-0.5}$	9.6 (9.3–9.9) $f^{+0.5}$	17	87
Ca	0.9 (0.8–1.0) $f^{-0.5}$	3.0 (2.7–3.3) $f^{+0.5}$	2.7	12
Fe	2.52 (2.46–2.59) $f^{-0.5}$	10.9 (10.7–11.2) $f^{+0.5}$	157	749
Ni	0.42 (0.39–0.47) $f^{-0.5}$	1.9 (1.8–2.2) $f^{+0.5}$	11	126

Table 8. Input and derived properties in the case of H-dominated plasma.

Property	ISM components		
	Low- T_e	Middle- T_e	High- T_e
kT_e (keV)	0.319 (0.314–0.326)	0.547 (0.541–0.552)	0.962 (0.957–0.967)
R (pc)	3.49	3.49	3.49
V (10^{57} cm^{-3}) ..	1.42	1.42	1.42
n_e (cm^{-3})	10.0 (9.7–13.5) $f^{-0.5}$	14.0 (13.9–14.2) $f^{-0.5}$	14.8 (14.7–15.0) $f^{-0.5}$
n_0 (cm^{-3})	2.1 (2.0–2.8) $f^{-0.5}$	2.92 (2.89–2.95) $f^{-0.5}$	3.09 (3.05–3.13) $f^{-0.5}$
E_t (10^{49} erg)	2.2 (2.1–3.0) $f^{+0.5}$	5.2 (5.1–5.3) $f^{+0.5}$	9.7 (9.6–9.9) $f^{+0.5}$
M_{swept} (M_\odot)	9.9 (9.6–13.4) $f^{+0.5}$	14.0 (13.8–14.1) $f^{+0.5}$	14.8 (14.9–14.6) $f^{+0.5}$
t_{ion} (yr)	100 (170–60) $f^{+0.5}$	$>1700 f^{+0.5}$	166 (172–160) $f^{+0.5}$

shown that the emission from ISM occupies the western region of the remnant. We therefore assumed that the plasma was compressed in the shell of the hemisphere with a radius and a thickness of $\sim 15''$ and $\sim 1.5''$, respectively. The shell thickness was taken from van der Heyden et al. (2002) and Lozinskaya (1992). Assuming a distance to LMC of 48 kpc (Macri et al. 2006), the radius and the thickness of the shell were estimated to be ~ 3.49 and ~ 0.35 pc, respectively. As a result, the volume of the plasma was estimated to be $V \simeq 1.42 \times 10^{57} \text{ cm}^3$. The obtained parameters are summarized in Table 8. In the ISM images for elements such as O and Fe-K (Figure 5), the morphology of this remnant is highly anisotropic. We emulated this effect by changing the volume filling factor f between 0.1 and 1.0 in order to estimate the number density, thermal energy, swept-up mass, and ionization age of the plasma.

Using the abovementioned values for the volume filling factor, the plasma number density of the low-, middle-, and high-temperature components were estimated to be ~ 10 – 32 , ~ 14 – 44 , and ~ 15 – 47 cm^{-3} , respectively. These plasma number densities were roughly consistent with the results obtained from XMM-Newton observations (~ 7 – 25 cm^{-3} : (van der Heyden et al. 2002)). Then, the pre-shock (ambient) number densities of the low-, middle-, and high-temperature components were estimated to be ~ 2 – 7 , ~ 3 – 7 , and ~ 3 – 10 cm^{-3} . These relatively high ambient number densities imply a physical connection to the HII region DEM L84 (Dunne et al. 2001) and the young rich cluster NGC 1850 (Chu & Kennicutt 1988) near this remnant. The complex images obtained with

Chandra/ACIS might reflect such a complex environment. We also confirmed that the supernova explosion for this remnant occurred in a high-density region with an ambient density of ~ 2 – 10 cm^{-3} .

The ionization ages of the low-, middle-, and high-temperature plasma components were estimated to be ~ 30 – 100 , >1700 , and ~ 50 – 170 yr, respectively, using the same assumption for the filling factor. These values are close to those obtained from XMM-Newton observations (van der Heyden et al. 2002). Rest et al. (2005) estimated the age of this remnant to be 860 yr based on the light echo. The age for the middle-temperature ISM component obtained in this study is consistent with this estimation. In contrast, the low- and high-temperature ISM components were estimated to be rather young at ~ 30 – 170 yr, suggesting that these two components might have been heated recently by the forward shock.

The total thermal energy was defined by $E_t^{\text{total}} = E_t^{\text{low}} + E_t^{\text{middle}} + E_t^{\text{high}}$, where E_t^{low} , E_t^{middle} and E_t^{high} denote the thermal energies of the low-, middle-, and high-temperature components, respectively. E_t^{total} was estimated to be $\sim 1.7 \times 10^{50} f^{+0.5}$ erg. Under the same assumption for the filling factor, the total thermal energy was estimated to be ~ 0.5 – 1.7×10^{50} erg, which is close to that of a general SNR (~ 0.5 – 7×10^{51} erg: (Hughes et al. 1998)). $M_{\text{swept}}^{\text{total}}$ was obtained by $M_{\text{swept}}^{\text{low}} + M_{\text{swept}}^{\text{middle}} + M_{\text{swept}}^{\text{high}}$, where $M_{\text{swept}}^{\text{low}}$, $M_{\text{swept}}^{\text{middle}}$ and $M_{\text{swept}}^{\text{high}}$ denote the swept-up masses of the low-, middle- and high-temperature components, respectively. In this case, $M_{\text{swept}}^{\text{total}}$ was estimated to be $38.7 M_\odot$. Assuming the same volume filling factor, the swept-up mass was estimated

to be 12.2–38.7 M_{\odot} . This high value indicates that the three-temperature plasma components essentially consist of swept-up ambient material.

6. Summary

We observed the supernova remnant N103B in the LMC with Suzaku and Chandra. In the spectral analysis conducted using Suzaku/XIS data, the diffuse thermal emission was closely reproduced with three ISM components with temperatures of ~ 0.32 , ~ 0.55 , and ~ 0.96 keV and the one ejecta component with a temperature of ~ 3.96 keV. The abundances of the ISM components were close to the LMC averages (Russell & Dopita 1992), and therefore we concluded that these components were heated by the forward shock. The ejecta component was overabundant in heavy elements such as Mg, Si, S, Ca, Fe, and Ni. Our interpretation is that this component originates from ejecta. The unprecedentedly high quality of the data allowed us to distinguish between ISM and ejecta emissions for the first time in a spectral analysis.

We also analyzed images obtained with Chandra/ACIS to examine the validity of the spectral analysis conducted with Suzaku/XIS data. We revealed that the distributions of elements from Si to Fe-K were similar to each other, although Fe-K was located slightly inward in comparison with lighter elements. This morphology supports our interpretation about ejecta-based emission. ISM emission (represented by O and Fe-L) is distributed differently than the ejecta emission. This morphology also supports our interpretation about ISM emissions. In addition, the ISM temperatures of ~ 0.32 , ~ 0.55 , and ~ 0.96 keV were significantly lower compared to the ejecta temperature of ~ 3.92 keV. These results indicate that the ejecta and ISM emissions were not dynamically connected (van der Heyden et al. 2002).

Combining spectral analysis based on Suzaku/XIS data and the high-energy continuum in the 5.2–6.0 keV band obtained with Chandra/ACIS, we showed the indication that the progenitor was most likely Type II. Assuming this progenitor type the progenitor mass was estimated to be 13 M_{\odot} based on the abundance patterns of Mg, Fe, and Ni relative to Si.

Based on the identification of the three ISM components from the single ejecta component, we also gained insight into the surrounding environment of N103B. The ambient number density for the three ISM components was estimated to be ~ 2 – 10 cm^{-3} . This relatively high ambient number density implies a physical connection with the HII region DEM L84 (Dunne et al. 2001) and the young rich cluster NGC 1850 (Chu & Kennicutt 1988) near this remnant. Thus, we revealed that the supernova explosion which gave rise to N103B occurred in a high-density region.

Acknowledgements

We thank the anonymous referee for fruitful comments. We also thank Y. Maeda, H. Yamaguchi, H. Yoshitake, I.

Mitsuishi, and T. Hayashi for many useful discussions and comments. We thank all members of the Suzaku team for their contributions to instrument preparation, spacecraft operation, software development, and in-orbit instrument calibration. We made use of archive data obtained from the *Chandra X-ray Center*, and we are grateful to the Chandra/ACIS team. This work was supported in part by a Grant-in-Aid for Scientific Research No. 22684012 (A. B) provided by the Japanese Ministry of Education, Culture, Sports, Science and Technology.

References

- Anders, E., & Grevesse, N. 1989, *Geochim. Cosmochim. Acta*, 53, 197
- Badenes, C., Harris, J., Zaritsky, D., & Prieto, J. L. 2009, *ApJ*, 700, 727
- Bamba, A., Yamazaki, R., Yoshida, T., Terasawa, T., & Koyama, K. 2005, *ApJ*, 621, 793
- Bamba, A., et al. 2008, *PASJ*, 60, 153
- Borkowski, K. J., Lyerly, W. J., & Reynolds, S. P. 2001, *ApJ*, 548, 820
- Borkowski, K. J., Sarazin, C. L., & Blondin, J. M. 1994, *ApJ*, 429, 710
- Chu, Y.-H., & Kennicutt, R. C., Jr. 1988, *AJ*, 96, 1874
- Chu, Y.-H., Kim, S., Points, S. D., Petre, R., & Snowden, S. L. 2000, *AJ*, 119, 2242
- Dickey, J. M., & Lockman, F. J. 1990, *ARA&A*, 28, 215
- Dunne, B. C., Points, S. D., & Chu, Y.-H. 2001, *ApJS*, 136, 119
- Filippenko, A. V. 1997, *ARA&A*, 35, 309
- Glatt, K., Grebel, E. K., & Koch, A. 2010, *A&A*, 517, A50
- Hamilton, A. J. S., Chevalier, R. A., & Sarazin, C. L. 1983, *ApJS*, 51, 115
- Hayato, A., et al. 2010, *ApJ*, 725, 894
- Hughes, J. P., et al. 1995, *ApJL*, 444, L81
- Hughes, J. P., Hayashi, I., & Koyama, K. 1998, *ApJ*, 505, 732
- Hughes, J. P., Rakowski, C. E., & Decourchelle, A. 2000, *ApJL*, 543, L61
- Hwang, U., Holt, S. S., & Petre, R. 2000, *ApJL*, 537, L119
- Ishisaki, Y., et al. 2007, *PASJ*, 59, 113
- Iwamoto, K., Brachwitz, F., Nomoto, K., Kishimoto, N., Umeda, H., Hix, W. R., & Thielemann, F.-K. 1999, *ApJS*, 125, 439
- Keller, S. C., & Wood, P. R. 2006, *ApJ*, 642, 834
- Kosenko, D., Helder, E. A., & Vink, J. 2010, *A&A*, 519, A11
- Koyama, K., et al. 2007, *PASJ*, 59, 23
- Lewis, K. T., Burrows, D. N., Hughes, J. P., Slane, P. O., Garmire, G. P., & Nousek, J. A. 2003, *ApJ*, 582, 770
- Liedahl, D. A., Osterheld, A. L., & Goldstein, W. H. 1995, *ApJL*, 438, L115
- Lopez, L. A., Ramirez-Ruiz, E., Huppenkothen, D., Badenes, C., & Pooley, D. A. 2011, *ApJ*, 732, 114
- Lozinskaya, T. A. 1992, New York: American Institute of Physics, 1992,
- Macri, L. M., Stanek, K. Z., Bersier, D., Greenhill, L. J., & Reid, M. J. 2006, *ApJ*, 652, 1133
- Mathewson, D. S., Ford, V. L., Dopita, M. A., Tuohy, I. R., Long, K. S., & Helfand, D. J. 1983, *ApJS*, 51, 345
- Mitsuda, K., et al. 2007, *PASJ*, 59, 1
- Nakajima, H. et al. 2008, *PASJ*, 60, S1

- Nomoto, K., Hashimoto, M., Tsujimoto, T., Thielemann, F.-K., Kishimoto, N., Kubo, Y., & Nakasato, N. 1997, *Nuclear Physics A*, 616, 79
- Rest, A., et al. 2005, *Nature*, 438, 1132
- Russell, S. C., & Dopita, M. A. 1992, *ApJ*, 384, 508
- Serlemitsos, P. J., et al. 2007, *PASJ*, 59, 9
- Someya, K., Bamba, A., & Ishida, M. 2010, *PASJ*, 62, 1301
- Uchiyama, H., et al. 2009, *PASJ*, 61, 9
- van der Heyden, K. J., Behar, E., Vink, J., Rasmussen, A. P., Kaastra, J. S., Bleeker, J. A. M., Kahn, S. M., & Mewe, R. 2002, *A&A*, 392, 955
- Vink, J., Kaastra, J. S., & Bleeker, J. A. M. 1996, *A&A*, 307, L41
- Yamaguchi, H., et al. 2008, *PASJ*, 60, 141
- Yang, X. J., Tsunemi, H., Lu, F. J., et al. 2013, *ApJ*, 766, 44